Laser-induced fluorescence velocimetry for a hypersonic leading-edge separation

4 authors, including:

Laurent Le Page
University of Oxford
21 PUBLICATIONS **44** CITATIONS

SEE PROFILE

S. L. Gai
Australian Defence Force Academy
143 PUBLICATIONS **1,228** CITATIONS

SEE PROFILE

Some of the authors of this publication are also working on these related projects:

AOARD FA2386-16-1-4014: Effects of Wall Temperature in High Enthalpy Rarefied Hypersonic Separated Flow View project

AOARD FA2386-19-1-4023: Wall Temperature and Bluntness Effects in High Enthalpy Hypervelocity Separated Flows View project

Physics of Fluids

Laser-induced fluorescence velocimetry for a hypersonic leading-edge separation

Laurent M. Le Page (ID), Matthew Barrett, Sean O'Byrne (ID), and Sudhir L. Gai (ID)

View Online   Export Citation   CrossMark

Laser-induced fluorescence velocimetry for a hypersonic leading-edge separation

Laurent M. Le Page,[a] (iD) Matthew Barrett,[b] Sean O'Byrne,[c] (iD) and Sudhir L. Gai[d] (iD)

AFFILIATIONS

School of Engineering and Information Technology, University of New South Wales, Canberra, ACT 2600, Australia

[a] Author to whom correspondence should be addressed: laurent.lepage@student.adfa.edu.au
[b] m.barrett@adfa.edu.au
[c] s.obyrne@adfa.edu.au
[d] s.gai@adfa.edu.au

ABSTRACT

Two-dimensional mapping of the velocity distribution for a hypersonic leading-edge separation flowfield generated by a "tick" shaped geometry is presented for the first time. Discrete measurements of two velocity components were acquired at a flow condition having a total specific enthalpy of 3.8 MJ/kg by imaging nitric oxide fluorescence over numerous runs of the hypersonic tunnel at the Australian Defence Force Academy (T-ADFA). The measured freestream velocity distribution exhibited some non-uniformity, which is hypothesized to originate from images acquired using a set of ultraviolet specific mirrors mounted on the shock tunnel deflecting under load during a run of the facility, slightly changing the laser sheet orientation. The flow separation point was measured to occur at 1.4 ± 0.2 mm from the model leading edge, based on the origin of the free shear layer emanating from the expansion surface. Reattachment of this free shear layer on the compression surface occurred at 59.0 ± 0.2 mm from the model vertex. Recirculating the flow bound by the separation and reattachment points contained supersonic reverse flow and areas of subsonic flow aligned with the location of three identified counter-rotating vortices. A comparison of the recirculation flow streamline plots with those computed using Navier–Stokes and direct simulation Monte Carlo (DSMC) codes showed differences in flow structures. At a flow time close to that produced by the facility, flow structures generated by the DSMC solution were seen to agree more favorably with the experiment than those generated by the Navier–Stokes solver due to its ability to better characterize separation by modeling the strong viscous interactions and rarefaction at the leading edge. The primary reason for this is that the no-slip condition used in the Navier–Stokes solution predicts a closer separation point to the leading edge and structures when compared to the DSMC solution, which affects surface shear stress and heat flux, leading to a difference in flow structures downstream of the separation.

I. INTRODUCTION

The development of high-speed cruise and atmospheric entry vehicles has motivated the investigation of the flow separation produced by the interaction between shock waves and boundary layers. These shock wave/boundary layer interaction (SWBLI) processes can occur on various components of these vehicles, such as control surfaces, and can be detrimental to both the integrity of structures and the overall vehicle performance. When considering flow separation at hypersonic Mach numbers, shock–shock interaction and SWBLI are challenging flow phenomena to predict accurately, particularly where flow density is sufficiently low

to allow velocity slip and temperature jump to occur in the flow adjacent to surfaces. Thermal nonequilibrium and strong rarefaction effects associated with hypersonic flow also contribute to their complexity. Consequently, there is a need for benchmark experimental data to validate computational models for these hypersonic viscous flows.

To this end, a leading-edge separation in a hypersonic flowfield is here considered for experimental study. This type of flowfield differs from the separated flow geometries used in previous work such as rearward facing steps,[1] compression corners,[2] and blunt bodies[3] in that the flow ideally expands and separates at (or near) the leading edge. The geometry used to produce such a leading-edge

separation is designated here as the "tick" arrangement and was first investigated by Chapman et al.[4] at supersonic Mach numbers. The rationale for using this configuration is that it minimizes the development of the boundary layer prior to flow separation, allowing the convenient analytical assumption of an initial zero-thickness boundary layer to be made. To date, only limited experimental data for this type of flowfield have been reported at hypersonic conditions.[5,6] The expected flow structures generated by this geometry are shown in Fig. 1. A shear layer initially sheds behind the separation point near the leading edge and divides the inviscid freestream flow from the slowly moving vortex in a recirculation region upstream of the reattachment point, and the pressure in this region reaches a plateau. A necking region of increasing pressure forms where the free shear layer reattaches to the surface, and a recompression shock wave forms downstream of this reattachment region.

Hypersonic wake flowfields have been investigated previously using hot-wire anemometry or model-mounted Pitot probes.[3] However, the flow disturbances caused by these physical probes interfere with the flow. By contrast, laser-based optical techniques can allow flow properties to be investigated without altering those flow properties. Examples of optical techniques include schlieren and shadowgraph imaging, which are line-of-sight experimental methods and have been used to quantify spatially averaged velocities of flow structures in hypersonic wake flows.[7,8] Laser-based techniques used in velocity measurements have also been successfully implemented in probing hypersonic flows. For example, Danehy et al.[9] measured a vertical velocity component in a separated flow behind a stepped cone, and Cecil and McDaniel[10] made velocity measurements on a flat plate. In this work, hypersonic flow with a specific total enthalpy of 3.8 MJ/kg is generated using a free-piston shock tunnel with a usable test time of up to approximately 1000 μs, limited by the drainage of flow through the nozzle. The low repetition rate of 4–6 tunnel runs per day and the limited available flow test time favor methods that can provide many data measurements during a single tunnel run.

Planar laser-induced fluorescence (PLIF) measurements meet the temporal accuracy and non-intrusiveness requirements mentioned above. Spatially resolved two-dimensional mapping of flow velocities is realized in this work using the laser-induced fluorescence of nitric oxide (NO), formed in measurable quantities by the reflection of an incident shock in the facility's nozzle plenum. The velocity field is calculated at every pixel by imaging

fluorescence using the Doppler-shift velocimetry technique.[11] The use of Doppler-shift velocimetry in hypersonic flows has been successfully implemented previously by Hruschka et al.[12] to map the velocity distribution of near wake flow behind a generic planetary entry probe by acquiring two-component velocity measurements. By mapping the velocity field using the PLIF technique, a new set of two-dimensional and spatially resolved velocity component measurements is available for comparison against computational simulations of the flowfield.

II. THEORY

The laser-induced fluorescence (LIF) technique is well understood, as is its implementation in hypersonic flow measurements from its combustion diagnostic origins.[13] LIF can be described as the process of a laser light source tuned to a resonance transition of an atomic or molecular absorber, exciting a certain fraction of the absorbing ground state population to a higher energy state. Part of the de-excitation process of the absorber is to spontaneously radiate (fluoresce) after some characteristic lifetime inherent to the excited state, returning to either the original or another lower energy state via a rovibronic transition. The complexity of this process is traditionally modeled using a two-level model of the molecular or atomic transition,[14] which incorporates the majority of important spectroscopic features of LIF. However, the two-level model omits supplementary processes such as rotational energy transfer (RET).[14] Other, more complex, models have been formulated, which can account for these supplementary processes.[15,16]

LIF can be applied as a point-wise technique but has been extended to a two-dimensional imaging method by using a planar sheet of laser light, in which form it is termed planar laser-induced fluorescence (PLIF).[12,17,23] The theoretical principles remain identical to LIF in that, at any pixel location within the imaged laser sheet, the total fluorescence intensity in the two-dimensional probed field is given by

$$S \propto N f_B B_{J''J'} E G \Phi C, \qquad (1)$$

where S is the fluorescence signal, N is the number density of the probed species, f_B is the Boltzmann fraction of molecules present in the lower state of the probed transition, $B_{J''J'}$ is the Einstein coefficient for photon absorption, E is the laser pulse energy, G is the spectral overlap integral of the laser line shape with the transition
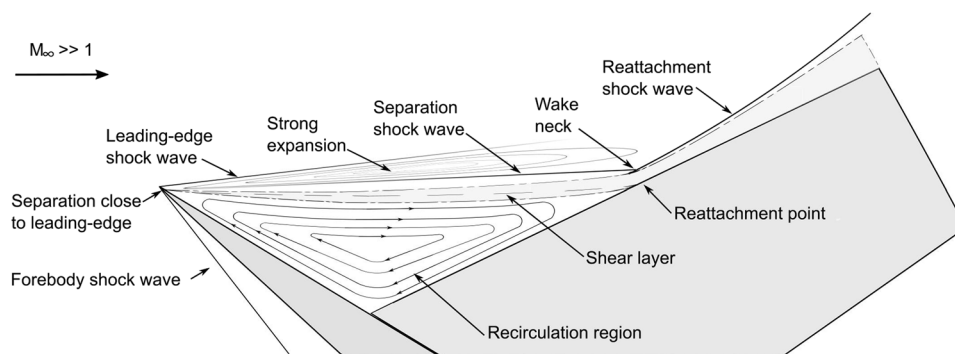

FIG. 1. Expected leading-edge separation flow structures.

line shape, Φ is the fluorescence efficiency, and C is a multiplicative factor that accounts for the optical collection efficiency of the detection system.[14]

A. Doppler-shift velocimetry

Velocity field mapping using laser-based methods has been performed previously using either time-of-flight techniques[18] or techniques based on the Doppler shift.[12] One time-of-flight technique is molecular tagging fluorescence velocimetry (MTV), first demonstrated by Hiller *et al.*,[19] which involves exciting a tracer species naturally present or seeded into the flow. This velocimetry technique is relatively simple, as the fluorescence lifetime is the only limiting parameter and does not require detailed knowledge of absorbing species spectroscopy. However, in a high quenching environment, MTV becomes a more difficult method to implement as the fluorescence lifetime reduces as the flow density increases. Velocities are determined from the distance traversed by the excited particles in a known time interval between the initial laser excitation and the subsequent fluorescence image. The precision of this method is determined by the fluorescence lifetime relative to the displacement of the excited fluorescence signal and the precision with which the center of the tagged flow region can be determined. Additionally, in hypersonic flows generated by impulse facilities, uniform seeding of the flow is difficult and the seeded molecules are often highly diffusive with respect to the advecting bulk flow. Other variants of time-of-flight techniques such as VENOM[20] and FLEET[21] cannot provide complete spatial information in the flowfield because of the need to measure displacement of the laser-tagged tracer line present in the flow.

These problems do not manifest using the Doppler-shift velocimetry method, provided an adequate concentration of a target species that can be excited with a laser source is present. This technique takes advantage of the fact that the bulk translational motion of an absorbing species will shift the spectral line shape peak from that expected in a stationary gas. This technique was first developed by Zimmermann and Miles,[22] and it has been successfully used and developed by other experimenters.[9,11,12] The Doppler-shift technique has two measurement approaches: the fixed-frequency[11,24] and tuned-frequency schemes.[23] The work presented here uses the latter approach to obtain velocity field mapping. The tuned-frequency scheme determines both the shape and position of the convolution between the laser and the candidate transition spectral line shape. This convolved line shape is achieved by scanning the laser wavelength over the spectral line center. The measured location of the spectral line center is Doppler shifted by λ_{DS} relative to the spectral peak of a zero-velocity reference λ_0 if the flow has a non-zero velocity component in the direction of the probed region. The Doppler-shifted line shape can be used to determine the flow velocity, V, using the expression

$$\lambda_{DS} = \lambda_0 \left(1 - \frac{V \cos \Theta}{c} \right), \qquad (2)$$

where c is the speed of light in vacuum and Θ is the angle between the vectors indicating the direction of the local flow and the direction of the laser beam's propagation. These line shapes are assembled piece-wise at each pixel from a set of fluorescence images, each of which is acquired at a different detuning of the excitation laser

wavelength from the center of a spectral line. The range of detuned frequencies used for these measurements is based on the highest expected flow velocity and temperatures in the flowfield, obtained, for example, through computational simulation of the flowfield. The Doppler-shifted line shapes are formed in this way because the shock tunnel facility used in these experiments has a limited test time and the laser system operating frequency is 10 Hz, allowing only one fluorescence image to be acquired per facility run. By fitting line shapes to intensities at every pixel location throughout the flowfield image, a velocity map of the flowfield is generated. A more comprehensive explanation of the Doppler-shift fluorescence velocimetry method and its implementation for high-speed flow is provided in Ref. 16.

III. EXPERIMENTAL ARRANGEMENT

A. Flow facility

Free-piston shock tunnels are facilities used to simulate the characteristics of hypersonic flight.[25,26] This type of facility, used to achieve high enthalpies and flow velocities, was first developed by Stalker in the 1960s[27] and involves heating of a driver gas by rapid quasi-adiabatic piston compression. The high Mach and Reynolds number flows generated in these facilities cannot be maintained continuously with test times of the order of a few milliseconds for large-scale free-piston shock tunnels. Smaller facilities such as the hypersonic tunnel at the Australian Defence Force Academy (T-ADFA) have a shorter turnaround time, which is particularly advantageous when developing experimental techniques or carrying out measurements that require a considerable number of facility runs. However, their usable flow test time is limited to the order of one millisecond or less at higher total enthalpy.

The T-ADFA free-piston shock tunnel at the University of New South Wales, Canberra, is one such smaller facility, being 17 m in total length. This facility is able to generate flows with total specific enthalpies of up to approximately 13 MJ/kg, with a usable test time of up to 1 ms, depending on the flow condition. The shock-heated reservoir gas feeds a 7.5° half-angle conical nozzle with a throat diameter of 12.7 mm, a length of 1100 mm, and an exit diameter of 305 mm. The effective nozzle half-angle accounting for the boundary layer displacement thickness along the nozzle walls is approximately 6.8°.[12] The usable central core flow, free from expansion or boundary layer effects, was approximately 220 mm based on a Pitot pressure survey.[5] A low-density flow condition where the continuum assumption holds for most of the flowfield, designated Condition E, is investigated here. This condition has a total specific enthalpy of 3.8 MJ/kg and a test time of approximately 1 ms. Additional thermodynamic quantities of this flow were computed using the one-dimensional inviscid chemical and vibrational nonequilibrium nozzle flow solver STUBE[28] accounting for boundary layer displacement corrections by matching computed and experimental Pitot pressures. The computed nozzle exit conditions are listed in Table I. The uncertainties cited in Table I arise from run-to-run fluctuations in measured pressures and shock speeds and do not account for any uncertainties in the sudden freezing model used to estimate vibrational freezing temperature or the chemical model used by STUBE. The freestream Knudsen number, $Kn_{\infty_{exp}}$, is taken relative to the model expansion surface length.

TABLE I. Nozzle exit aerothermodynamic parameters and model leading-edge radius dimension.

Parameter	Condition E
Rotational temperature (K)	156 ± 8
Freestream pressure (Pa)	310 ± 60
Freestream velocity (m s^{-1})	2490 ± 10
Freestream density (kg m^{-3})	$(7 \pm 1) \times 10^{-3}$
Freestream Knudsen number ($Kn_{\infty_{\text{exp}}}$)	0.000 42
Equilibrium specific heat ratio, γ	1.30
Mach number (frozen)	10.3 ± 0.3
Unit Reynolds number (m^{-1})	1.34×10^{6}
Nozzle exit NO mole fraction	0.050
Leading-edge radius (μm)	20 ± 10

B. Test model

The leading-edge separated flowfield studied here is generated using a model consisting of two angled flat plates arranged in a "tick"-shaped configuration. This model geometry, first suggested by Chapman et al.,[4] was chosen for this study as it produces a near zero-thickness boundary layer prior to separation, making the separated flowfield more amenable to analytical approaches that assume zero initial boundary layer thickness, as Chapman's original analyses do. This arrangement can be considered as a limiting case of separation both behind a base and a compression corner, and only recently interest has been expressed in this geometry for the investigation of low-density separated flow.[6,29,30]

This model has a removable leading-edge component that is changed regularly to reduce blunting effects or damage caused by burst diaphragm debris. The leading-edge radius used is 20 ± 10 μm, based on the range of measurements for each of the leading edges, and is indicative of machining repeatability of the leading edges. Its stationary position relative to the centerline of the facility's nozzle exit is 35 ± 1 mm for these experiments. The model aspect ratio of 10 was designed to minimize the possibility of three-dimensionality

in the recirculating vortex, the location of all experimental measurements.

As the leading-edge radius is an important parameter and strongly influences the downstream flow structures,[31,32] the leading edge was monitored throughout the experimental campaign. Using a Zeiss Stemi SV8 stereomicroscope, a graduated microscope slide was imaged with the leading-edge radius to compare dimensions at the longitudinal centerline, corresponding to the laser sheet location on the model, after every ten runs of the facility. If the measured dimension did not match the nominal manufactured radius, the leading-edge was replaced. To reduce the likelihood of the model underside generating shock–shock interactions for these experiments, which could create a disturbance near the model leading edge and detach the leading-edge shock wave, an extended bevel length was employed to ensure no geometric underside discontinuities, as shown in Fig. 2. A long recompression surface was chosen to ensure that the expansion of the flow around the downstream corner would not influence the separated flow.

C. Fluorescence imaging system

The PLIF laser system is identical to the configuration used in a previous shock tunnel experiment investigating hypersonic wake flows.[12] The system consists of a narrowband dye laser (Lambda Physik Scanmate 2E) pumped by the third harmonic of a Q-switched Nd:YAG laser (Quantel YG-981E). The dye laser uses a Coumarin 2 dye producing light at 452 nm and is fitted with a type 1 β-barium borate (BBO) frequency-doubling crystal to produce pulsed, tunable radiation around 226 nm, which overlaps with the NO $A^2\Sigma^+ \leftarrow X^2\Pi$ $v'' = 0$ system of rovibronic transitions. An intra-cavity etalon was installed in the dye laser cavity, which reduces the laser spectral linewidth to 0.59 ± 0.02 pm according to low-pressure gas cell measurements and constrains the longitudinal laser mode envelope. The frequency-doubled laser beam is sent from an optical table to the sheet-forming optics, located above the facility test section, via a series of UV dielectric mirrors. The beam was passed through a 20 mm focal length plano–convex cylindrical lens and a spherical lens of 1000 mm focal length to form the beam into a sheet
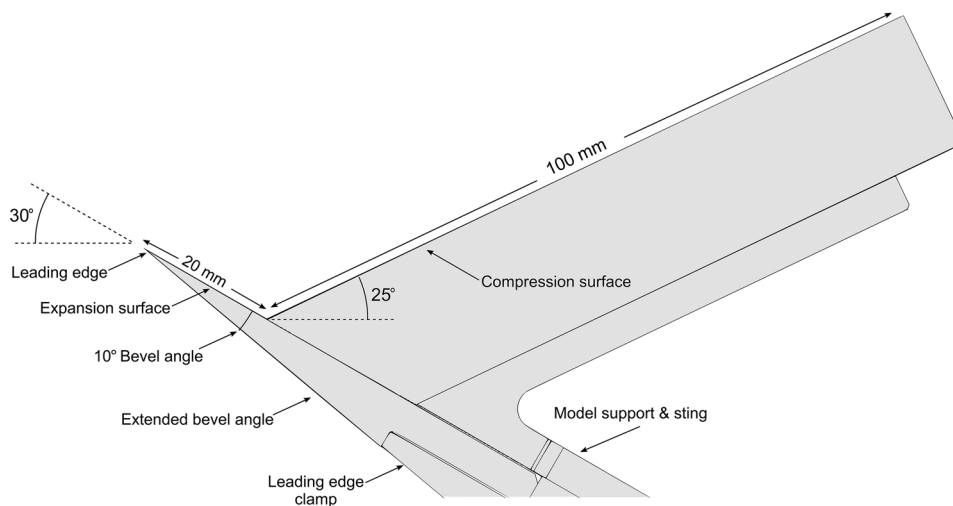
FIG. 2. Tick test model configuration.

that was 0.8 ± 0.2 mm thick. An apertured beam splitter located 30 mm above the test section truncated the sheet width to approximately 70 mm for radial velocimetry experiments and 35 mm for axial velocimetry experiments. The reason for the reduced sheet width for the axial velocimetry was to allow a similar portion of the background intensity to be imaged, which was then subtracted from the acquired image. Light reflected by the beam splitter was directed to a dye cell containing a saturated solution of Rhodamine 6G in methanol. The fluorescence from the dye cell was imaged using a 10-bit monochrome CCD camera (MicroPIX M640), providing a signal proportional to the spatial energy distribution and dimensions of the laser sheet in the facility's test section, as the distance from the beam splitter to the nozzle axis was identical to the distance from the beam splitter to the dye cell. The transmitted laser light through the first UV mirror—approximately 3% of the total beam energy—was measured using a Thorlabs DET25K GaP biased photodiode and was used to calibrate the total beam energy. Wavelength tuning to a candidate transition was done by recording the fluorescence generated in a room temperature, 500 Pa, pure NO gas cell, using a photomultiplier tube. Laser pulse energy measured using the Thorlabs UV photodiode was calibrated against an Ophir PE25 laser power meter positioned upstream of the final UV mirror that directed the beam into the sheet-forming optics.

The NO fluorescence in the shock tunnel was imaged using a Stanford Computer Optics 4Picos intensified CCD (ICCD) camera. Both the ICCD and sheet profile cameras were calibrated for response linearity across the expected range of fluorescence intensities, and the ICCD camera gain response was calibrated over a range of gain voltage values, allowing images captured at different gains to be converted to the same gain level. The scattered laser light from the model surfaces or from particles in the flow was filtered by using a Schott UG5 filter, and a narrowband dielectric mirror with maximum reflectivity at 308 nm was used to remove UV emission from the flow between wavelengths of 285 nm and 335 nm, where there are strong atomic lines, particularly from Fe atoms liberated in the shock reflection process. This combination of filtering optics allowed only the fluorescence from the higher NO vibrational bands to be imaged. During a run of the facility, the laser and image capture systems were synchronized relative to the pressure rise after shock reflection in the shock tunnel plenum. Upon receipt of this trigger, a single laser pulse synchronized with the flow arrival was sent to the test section and the resulting fluorescence image, laser pulse energy trace, and sheet profile image were acquired. As the maximum operating frequency of the pump laser is 10 Hz, only one fluorescence image was obtained for each run of the facility. The raw fluorescence images were processed following the approach of Seitzman _et al._[33] and were corrected for background noise, laser sheet spatial energy variation, and total laser pulse energy. The ICCD camera dark noise was subtracted from each fluorescence image, followed by an image background subtraction taken from the mean intensity level of several columns on the left side of the image (outside the laser sheet excitation), which was removed from all pixels to account for shot-to-shot variations in the background luminosity. A seventh-order polynomial fitted to the laser sheet profile spatial energy distribution was used to normalize the laser intensity distribution in the PLIF image. Dividing each image column by its relative energy and then taking the quotient of all pixel intensities,

and the total laser pulse power, corrected each image to a uniform laser energy. This assumes linear fluorescence response, but the laser irradiance was limited to values where this assumption is correct.

IV. EXPERIMENTAL RESULTS

For all velocity measurements, a range of laser detunings in the vicinity of the $^{R}R_{22}(13.5)$ transition were probed. This transition was chosen because it was an isolated spectral line that had a reasonable signal for the range of conditions expected in the flowfield. Two velocity components, named for convenience the radial and axial components, were probed in separate experiments. Due to differing ranges of the expected velocities for these velocity components, the range of detunings centered on the spectral peak of $^{R}R_{22}(13.5)$ line span from −1.7 to 1.7 pm and from −1.8 to 3.3 pm for the radial and axial velocity components, respectively. The radial component is captured with the laser sheet propagating perpendicular to the freestream flow direction or radially with respect to the nozzle exit diameter. For the axial velocity component, fluorescence images were captured using the laser sheet propagating at an angle parallel to the model's compression surface due to restriction in optical access to probe the axial component directly: a sheet that was oriented in the horizontal direction would be obscured by the model. The beam also cannot be oriented parallel to the expansion surface because the laser sheet would be obstructed by the nozzle. This optical restriction was caused by the model compression surface obscuring the laser sheet, which necessitated using an arrangement consisting of two aluminum front-surface mirrors that were installed in the T-ADFA test section. The two mirrors were oriented and set to direct the laser sheet parallel to the model's compression surface, and the existence of these mirrors in the test section did not adversely affect the oncoming freestream, with no flow perturbations observed during image acquisition. Aluminum front-surface mirrors were selected for their high reflectivity at ultraviolet wavelengths and to remove any potential secondary reflection from the glass substrate. These mirrors were changed for each run of the facility because of ablation damage from particulates in the hypersonic flow. An axial view of this mirror arrangement installed in the T-ADFA test section is shown diagrammatically in Fig. 3.

By probing the flow at an angle parallel to the model compression surface, this required an additional calculation in post-processing to determine the axial velocity measurement rather than the velocity component along the laser propagation direction. This was done by dividing the calculated velocity value determined along the laser propagation direction by the cosine of the laser sheet angle to the horizontal axis to obtain the axial velocity component measurement, which is henceforth referred to as the axial velocity. The laser sheet angle of 25° ± 0.5° was set for the duration of the axial velocimetry experiments to match that of the tick model compression surface. The angle uncertainty of ±0.5° corresponds to the velocity uncertainty of approximately 1%.

Forty eight acceptable NO–PLIF images were acquired for the radial component, and forty image usable camera frames were recorded for the axial component, with a minimum of two images captured for each detuning. Images captured at these laser detunings were obtained in a randomized order to minimize systematic error.
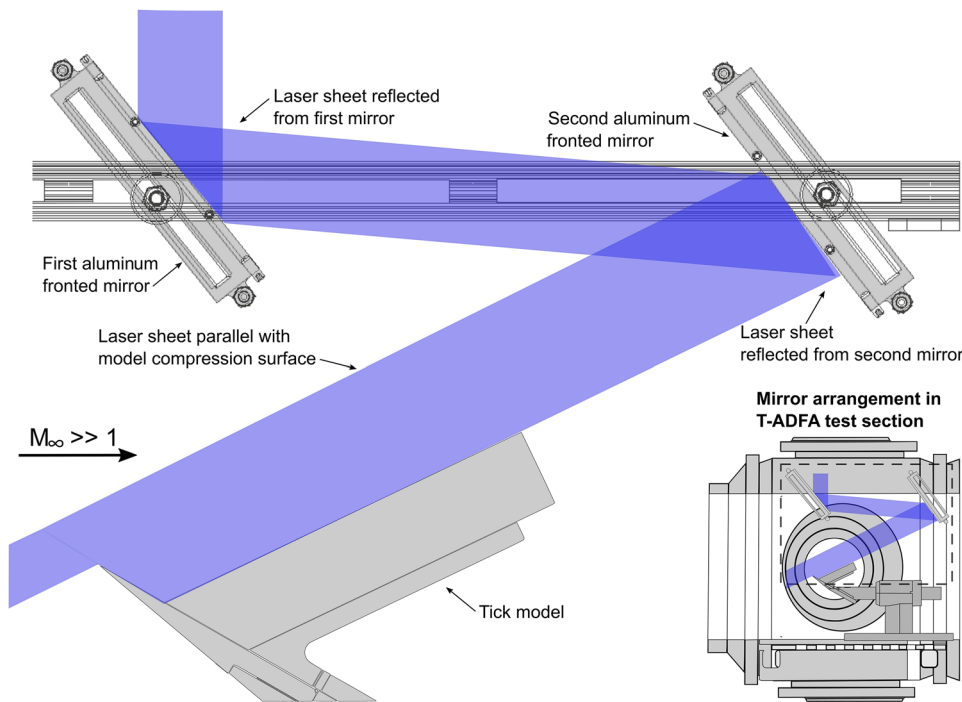
FIG. 3. Axial velocity mirror arrangement in the T-ADFA test section.

The criteria for image acceptability to be used in calculation were based on several factors that could change either the imaged flow, such as debris striking the leading-edge, or collisional quenching effects that could introduce systematic error into the velocity measurement. These include monitoring shock tube pressure for each run to ensure that the nominal flow conditions did not deviate significantly from run-to-run and also checking for image saturation by comparing the mean fluorescence signal from the top of each image against the sheet profile image. The total laser pulse energy was monitored at the laser emission aperture before each run to ensure consistent excitation energy, which was measured to be $900 \pm 100 \ \mu J$ for all experiments. The laser sheet energy was also recorded using a 10 mm section from its center, which was not permitted to drop below $30 \pm 5 \ \mu J$. A small portion of the sheet was used for monitoring due to the limited size of the detector and the energy distribution across the laser sheet also being approximately uniform. Immediately prior to operating the facility, the laser was tuned to the selected detuned frequency using a photomultiplier tube measurement from a low-pressure pure NO gas cell. To ensure that the captured image corresponded to the desired wavelength, a subsequent scan immediately after the run was performed to confirm that the laser was still tuned to the correct frequency. Approximately 30% of the acquired PLIF images were omitted due to one or more of these checks not meeting their respective criteria, and the affected acquired image was not used in the subsequent velocity calculation.

Gaussian line shape functions, appropriate for the low-pressure environment investigated here, were fitted to individual pixel intensities in each of the images that were acquired at different laser detunings. The Gaussian curve represents a convolution of the laser and transition line shapes whose Doppler-shifted line center is referenced to a similar measurement of static gas in a NO gas cell.[9,11,24] The deviation of the peak center position from the reference line center was used in Eq. (2) to determine the velocity at each pixel. The fitted peak line center position, from which the velocity is determined, remains unaffected by the selection of line shape function, which has been discussed by Danehy *et al.*[9] who used Voigt functions for fitting and found that no significant difference could be observed.

A. Velocity component measurements

Prior to presenting the velocity field of the studied flow, some notable aspects of each velocity component measurement are briefly discussed. As the radial velocity was probed using a vertically oriented laser sheet orthogonal to the oncoming freestream, the Doppler shift is sensitive to the velocity component in the vertical or radial direction. The radial component of the freestream velocity is relatively small compared with the axial component and is similarly the case within the recirculating vortex. As the freestream is processed by the recompression shock wave and the separated flow is directed parallel to the model compression surface, the radial velocity magnitude becomes appreciable. The freestream flow exiting the facility nozzle expands as a function of radial and axial distance, so the radial velocity component magnitude should increase from a near zero velocity close to the nozzle centerline (located at the model leading edge) to a higher magnitude. This has been captured in the radial velocity measurements, shown in Fig. 4 as a radial velocity profile taken from the mean velocity within a 3 mm wide vertical strip taken parallel to the leading edge encompassing a length of approximately 40 mm to just below the top of the image frame
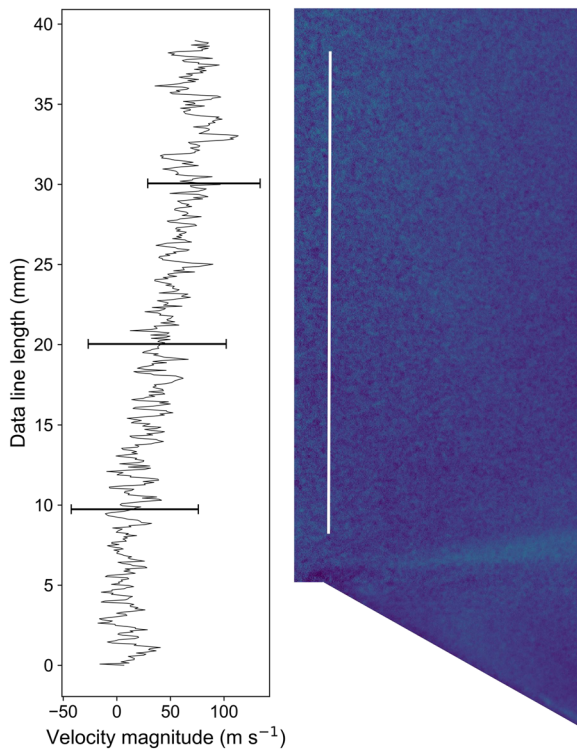
FIG. 4. Radial velocity profile of Condition E freestream.

axial experiments. However, the peak freestream velocity of approximately 2500 m s^{-1} coincided with the axial velocity predicted by using the one-dimensional nozzle code, STUBE.[28] Additionally, during the 100 ns gating time for fluorescence imaging, the freestream will advect downstream by 0.25 mm during the exposure. It is possible that this could cause some partial image blurring in the high-speed flow regions across what is the equivalent of approximately 4 pixels and may be a small additional source of uncertainty for measurements in the freestream. Motion blurring is not significant for the separated and reattaching flows as velocities are significantly below the freestream value.

The calculated freestream axial velocity located near the recompression surface exhibited a region of reduced velocity magnitude that emanated from near the expansion fan and that runs parallel with the recompression surface through to the imaged flow edge. As with the freestream velocity discrepancy near the leading edge, it would be expected that the freestream would be approximately uniform in this area. The source of the velocity difference in this region compared to the peak freestream velocity arose from the corrected fluorescence images captured at various laser detunings, which exhibited non-uniformity of the imaged fluorescence signal within the freestream. The most severe example of this was seen in fluorescence images acquired at 1.5 pm and 1.8 pm laser detunings, which are shown in Fig. 5. The signal distribution shown in Fig. 5(a), the 1.5 pm image, where the freestream fluorescence is only seen as a strip near the compression surface, was captured repeatedly across all images at this detuning. Several images acquired at the 1.8 pm detuning also had an abnormal signal distribution as shown in Fig. 5(b), where only a strip of appreciable signal was observed from approximately the freestream mid-point to the image periphery. This fluorescence distribution was only seen in another 2.4 pm detuned image, with subsequent images at this detuning having distribution similar to Fig. 5(b). After image acquisition at these wavelengths, the experimental arrangement was checked for damage or unwanted movement in the mirror array from the flow, which would modify the laser sheet orientation during image acquisition. These checks uncovered no adverse modification to the mirror arrangement after a facility run, and the laser sheet was also in its nominal position. The cause of these variations in the fluorescence distribution is not precisely known. It is hypothesized that the second mirror that faces the oncoming flow, in particular, may sometimes deflect in the mirror mount during a run of the facility, altering the laser sheet propagation path. As fluorescence images are captured at a time late in the overall flow time, there is ample opportunity for the flow to interact with the mirror, dynamically altering its position by a small increment. The irregular fluorescence patterns were not seen consistently for each PLIF image and laser detuning. It is

indicated on the zoomed-in map by the vertical white line. As can been seen in this plot, the radial velocity magnitude increases from approximately 0 to 100 ± 20 m s^{-1} as a function of radial distance from the nozzle centerline as the flow expands. This demonstrates the Doppler shift measurement's ability to resolve low velocity magnitude (below 100 m s^{-1}) in the direction of laser sheet propagation. Further samples of similar velocity profile measurements of this flowfield can be seen in a recent article by Prakash *et al.*[34]

An observed feature of the calculated axial velocity distribution from fluorescence measurements was that the freestream magnitude did not appear to be completely uniform across the probed region, particularly close to the model leading edge where one would expect the velocity to be approximately equal to the velocity further downstream. One reason for this is a poor signal-to-noise ratio for pixels in this region, attributed to increased laser sheet attenuation or absorption due to the extended optical path of 0.34 m for the

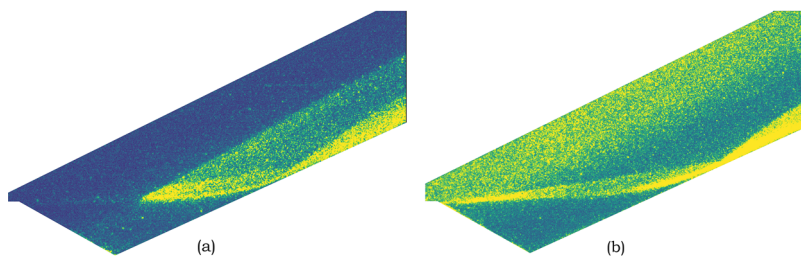**FIG. 5**. Freestream fluorescence variation at (a) 1.5 pm laser detuning and (b) 1.8 pm laser detuning.

believed that mirror fastening to each mount may not have been secure enough to prevent mirror deflection for some measurements or the replaced mirror substrate thickness variance of approximately 4 mm contributed to the effect on laser sheet orientation.

V. VELOCITY FIELD

An overall map of the separated flowfield velocity magnitude, $V_{mag,px}$, is shown in Fig. 6. This map was generated using the calculated orthogonal radial, $V_{rad,px}$, and axial, $V_{ax,px}$, velocity components determined from the imaged fluorescence at every pixel via calculation of the Pythagorean theorem,

$$V_{mag,\,px} = \sqrt{V_{ax,px}^2 + V_{rad,\,px}^2}. \quad (3)$$

As has been noted, the axial velocity component, $V_{ax,px}$, used in this calculation is determined by dividing the velocity measurement taken along the compression surface by the cosine of the laser sheet angle to the direction of the freestream flow in the center of the nozzle. By doing this calculation, the use of Eq. (3) is valid as the radial and axial velocity components are the orthogonal axial and radial components of the flow relative to the freestream direction. As the imaged freestream fluorescence for the axial case differed in proportion to the radial velocity measurements, the calculation of velocity magnitude was limited to the laser sheet dimensions used to probe the axial velocity component. Additionally, the axial component is the dominant velocity vector in the freestream flow, and the magnitude map in Fig. 6 closely resembles the axial velocity component distribution.

The flow velocity detail at the separation point in Fig. 6 has been somewhat obscured by the measurement noise due to laser scatter at the model leading-edge surface, which generates unrealistic velocity values close to the surface. However, extrapolating where the shear layer separates near the leading edge is a good indicator of the separation position. Using this location, the flow separation point is estimated to occur at approximately 1.4 ± 0.2 mm from the leading edge along the expansion surface. Following the free shear layer downstream, flo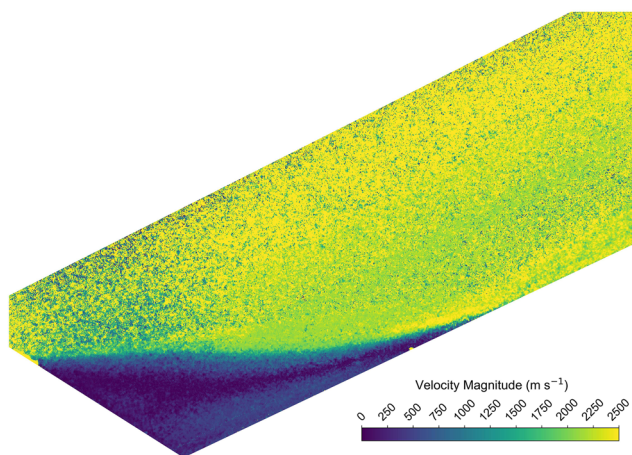w at its reattachment that is not ingested into the recirculation region is directed through a wake neck characteristic of large-scale hypersonic separated flows downstream of reattachment to a surface.[35] The viscous flow here traverses the neck where the velocity magnitude peaks at approximately 2500 m s^{-1}. Downstream of the wake neck minimum height, the flow is slowed after being processed by the recompression shock wave. The maximum height in the imaged area of the recompression flow from the model surface to the outer edge of this shock layer is 7.2 ± 0.2 mm, although this could continue to grow, given a wider field of view or a sufficiently long recompression surface. Flow across the wake neck region can be considered to act analogously to a longitudinally halved de Laval nozzle, with the minimum neck area being equivalent to the nozzle throat.

Looking to the recirculating flow bound by the shear layer separation and reattachment points, an area of high magnitude flow is seen running back upstream toward the model vertex along the compression surface indicated by the lighter region in the color-map. This area coincides with the reverse flow seen in data taken from the axial and radial components, which is shown in Fig. 7. The reverse flow source is from the reattaching shear layer diverting a portion of the flow in both the upstream flow direction and downstream flow direction, which is then compressed by the reattachment shock wave. The reverse flow propagation resembles the jetted flow that partially expands into the recirculating cavity at an average supersonic Mach number of 1.84, extending from downstream of the necking region to approximately the model vertex. Remaining in the recirculation region, the subsonic flow indicated by the darker areas in the color-map is seen to run upstream of the vertex and then across the upper region of the recirculating flow, which is below 240 m s^{-1}, through to the reattachment point where the recirculation flow also entrains fluid from the shear layer.

To illustrate the flow path(s) of the separated flowfield, a streamline plot magnified on the cavity recirculating flow has been superimposed on the velocity magnitude map, which is shown in Fig. 7. These streamlines have been determined by taking the curl of the velocity measurements. The freestream flow and recompressing flow have been truncated from this figure to focus on the cavity flow structures, which exhibit a complex flow geometry that encompasses the entire region from the flow separation through to the wake neck.

The obvious feature in this figure is a large primary vortex seen approximately in the upper center of the flow in the cavity formed by the expansion and recompression surfaces. This primary vortex appears to be partially fed from the fast flowing reverse flow
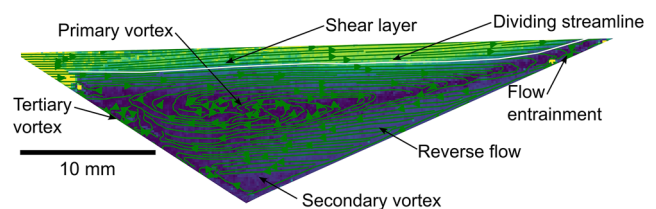

FIG. 6. Separated flowfield velocity magnitude map.

FIG. 7. Separated flowfield streamline map superimposed over the velocity magnitude, where the dividing streamline is shown in white.

emanating from the flow entrainment at the shear layer reattachment point. The streamlines seen in this region have a significant axial flow component, and a single streamline in this reverse flow is seen running parallel close to the surface, suggesting boundary layer development of the reverse flow. The primary vortex is also fed from the flow at the separation point with streamlines seen emanating from the beginning of the dividing streamline (indicated by the white streamline) and running in the inviscid streamwise direction, with some of these streamlines merging with the top side of this vortex. With the two sources of flow entrained into this primary vortex traveling in opposite directions, being left to right from the separation and right to left from the reattachment, the primary vortex rotation direction is clockwise, as expected, driven by the momentum of the freestream flow adjacent to the shear layer. The span and position of the primary vortex also coincide with the large subsonic region indicating that the primary vortex is rotating at a constant velocity rather than being driven by shear, looking at the color-map superposition.

A secondary vortex can also be seen located in the corner or model vertex, which is also fed by the upstream reverse flow running along the compression surface. The location of this feature is offset by 1.7 ± 0.2 mm downstream from the geometric corner or vertex of the model. Streamlines seen above this structure that are not entrained into the primary vortex turn at the expansion surface with the flow then running toward the corner. Although there is sparse streamline density in this area, the secondary vortex is seen to be rotating in a counter-clockwise direction, opposite to the rotation direction of the primary vortex. Further upstream of this structure, along the expansion surface and in front of the primary vortex, a tertiary vortex forms approximately 8 mm from the leading edge. Looking at the oncoming streamlines from the reverse flow, it appears that the flow not entrained into either the primary or secondary vortices partially feeds this small vortex, which is driven in the counter-clockwise direction. On the upstream side of this vortex, there is a lack of streamlines originating from near the separation to illustrate this definitively. However, a solitary streamline is seen flowing from near the leading edge, which turns by almost 180° to coalesce with streamlines in the small vortex, suggesting another source to drive the vortex rotation from the upstream side from the separation point. This tertiary vortex location corresponds to another area of subsonic flow near the expansion surface indicated by the dark area on the color-map, with an average Mach number of 0.31 using averaging from a 30×30 pixel area.

Another detail captured in this streamline plot is the flow entrainment location at, or near, the reattachment. Looking at the extreme right of Fig. 7, an arrowhead is seen turning to face the compression surface. Streamlines near this point are also turned and indicate that the flow is running along the compression surface back toward the model vertex. Streamline density may not be sufficient to accurately identify the precise location of the recirculation flow entrainment from the shear layer, but from what is seen here it appears that this location is approximately 59 ± 0.2 mm along the compression surface from the model vertex.

The dividing streamline is an important flow feature that describes the boundary of the flow that is entrained into the recirculation and the flow that continues downstream of the reattachment. The location of the dividing streamline is shown as the white streamline in Fig. 7. The laminar mixing theory outlined by Chapman[36] states that, for a leading-edge separation, the velocity along the dividing streamline, U_{DSL}, remains constant and has a specific velocity ratio to that of the freestream, U_∞, given by

$$\frac{U_{DSL}}{U_\infty} = 0.587. \qquad (4)$$

This ratio is said to vary slightly with flow Mach and Reynolds numbers or with the length of the dividing streamline.[4] This velocity ratio has been measured previously using experimental data from a PLIF-based investigation of a hypersonic base flow by Hruschka et al.,[12] which was found to be 0.34, significantly lower than the prediction by Chapman et al.[4] This was because Chapman et al.[4] applied this theory to supersonic flows and the base flow of Hruschka et al.[12] had a developed boundary layer prior to separation. The velocity magnitude map in Fig. 6 can be used as a more direct comparison as the model configuration is identical to that analyzed by Chapman et al.,[4] as the free shear layer is encountering a wall at the reattachment, as opposed to the coalescing shear layers in the wake of a base, which will have differing flow shear stress at the reattachment.[37] Figure 8 shows the dividing streamline velocity ratio taken from the separated flow velocity magnitude. The extracted data of the dividing streamline were taken to be at the recirculating flow and freestream interface indicated by the low velocity magnitude and an increase in the freestream value. The data span from near the leading edge—omitting the laser scatter noise—through to the reattachment/necking region. The velocity magnitude along the dividing streamline was used in the velocity ratio with the averaged freestream velocity taken from a 100×100 pixel region. As can be seen in Fig. 8, there is some variability in the value of U_{DSL}/U_∞ from pixel to pixel. If one were to consider the mean U_{DSL}/U_∞ indicated by the solid horizontal line in Fig. 8, which is equal to 0.511 ± 0.100,
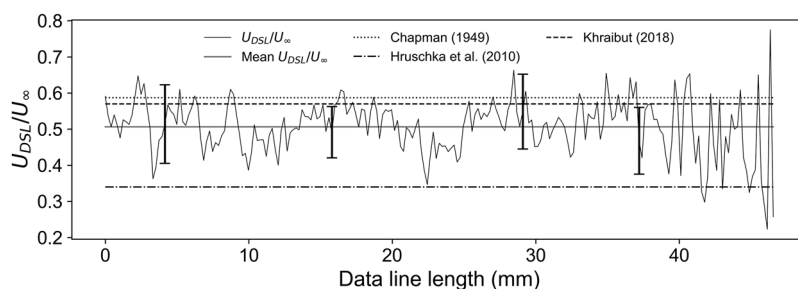

FIG. 8. Dividing streamline velocity ratio, U_{DSL}/U_∞.

then this ratio is less than the predicted value of 0.587 but clearly is in better agreement than the $U_{DSL}/U_\infty = 0.34$ from the data of Hruschka et al.[12] for the dividing streamline velocity in the separated region of a base flow, also shown in Fig. 8. This is an indication of the need to remove the boundary layer effect on the dividing streamline velocity and reinforces the assumption that the tick configuration is closer to Chapman's idealized free shear layer model than a base flow where the boundary layer has a non-negligible initial value. The $U_{DSL}/U_\infty = 0.57$ value for the tick flowfield determined from the steady-state Navier–Stokes computation by Khraibut et al.[29] is closer to the value of Chapman et al.[4] The difference in the tick flow with both calculations is within the measurement uncertainty of the experiment. It is important to note that neither Chapman's analysis nor Khraibut's computations account for the possibility of slip in the separated flow.

The discrepancy here should be considered with the caveat that Chapman's theory is only applicable for steady two-dimensional flow separation where no boundary layer exists prior to separation.[4,38] Chapman et al.[4] states that if an appreciable boundary layer thickness exists prior to separation, the velocity profile would alter and the value of U_{DSL}/U_∞ would not be equal to 0.587. Baum and Denison[38] developed Chapman's model further to include a boundary layer of finite thickness, assuming that the base of the body is sufficiently large compared to the thickness of the shear layer. This assumption also uncouples their U_{DSL}/U_∞ from the Reynolds number. From this model, the velocity ratio assuming that the dividing streamline velocity is not equal to that of the freestream is

$$\frac{U_{DSL}}{U_\infty} = \sqrt[3]{3S^*}, \tag{5}$$

where S^* is the length of the dividing streamline from the separation point through to reattachment. As a small yet finite boundary layer does exist for the separated flow studied here, this velocity ratio is more applicable for comparison. When specifying S^* as the length of data extracted from the shear layer, the U_{DSL}/U_∞ ratio is equal to 0.511, an exact match to that of the mean experimental velocity ratio. This also coincides with an analytical prediction by Baum and Denison[38] for the value of S^* given in their article. The separated flowfield computation by Ref. 29 is also closer to the experimental value using the model of Baum and Denison.[38]
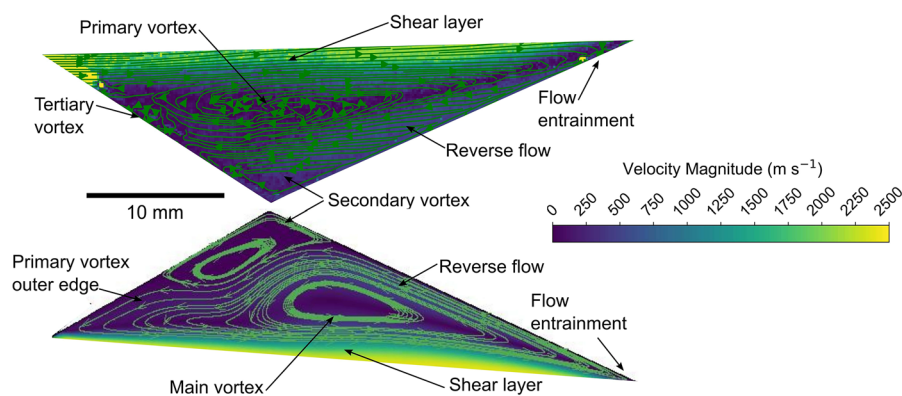
A. Numerical simulation comparison

1. Navier–Stokes computation

The experimental measurements of this separated flow are compared to both a steady-state Navier–Stokes solution and a direct simulation Monte Carlo (DSMC) computation. First, a two-dimensional and steady-state Navier–Stokes numerical simulation result computed by Khraibut[29] using the US3D code[39] is compared to the experimental flowfield, focused on the cavity flow only. The leading-edge radius in this computation is set to 15 μm, making it close to the experimental value of 20 ± 10 μm. This comparison is shown in Fig. 9 and is presented with the experimental streamline plot superimposed on the velocity magnitude map mirrored with the equivalent result from computations.

Importantly, the experimental and computed flow structures in the recirculation bubble differ considerably. To focus on the comparison in this region, a magnified view is shown in Fig. 9. Although the overall size of the separated region between the two cases is similar, the simulation extends further downstream and the most obvious difference is the primary vortex position in the separated region. In the experimental results, this flow feature resides in approximately the center of the recirculating flow, whereas in the Navier–Stokes computation, the primary vortex center is offset by approximately 7 mm downstream from the corner. The primary vortex size also differs with the numerical result spanning horizontally from the shear layer flow entrainment at reattachment through to near the separation point, indicated by the primary vortex outer edge label in the figure. Streamlines in the experimental map also show that the primary vortex encompasses a horizontal region spanning from near the reattachment but instead is truncated approximately 8.4 mm from the leading edge.

The reverse flow feeding the primary vortices contributes to this size and possibly the position discrepancy, although as the computation is that of a steady state, a direct comparison of the flowfield at the same instant in time is not possible. In the numerical case, the reverse flow seems to traverse parallel to the compression surface, whereas in the experimental measurements, this reverse flow has a distinctly larger axial velocity component. This higher axial flow magnitude in the experimental case looks to truncate the primary vortex height by running more horizontally and further underneath the primary vortex. This also affects the secondary vortex size in the experimental case as the almost horizontal flow

FIG. 9. Experimental separated flowfield streamline map (top) mirrored with equivalent Navier–Stokes computation (bottom).

also restricts its size. As the reverse flow in the computed flowfield runs along the compression surface, this truncation of either vortex is not seen and the secondary vortex is permitted to grow along the expansion surface. It should be noted that these two vortices in the experimental and numerical cases rotate in identical directions, which are clockwise for the primary vortex and counter-clockwise for the secondary vortex evident in the experimental velocity map. The difference in the downstream flow structure in the experimental case clearly plays a role in the formation of this small flow feature. Notably in the numerical case, there are no streamlines emanating from the separation and flowing downstream as in the experimental map, only fluid running upstream as a part of the primary vortex. Flow from, or near, the separation point seems to only flow close to the dividing streamline in the recirculation, feeding the primary vortex. There is also no evidence in the numerical results of the existence of a tertiary vortex, which could be indicated by bulging streamlines in the vicinity of the expansion surface. With the large span of the numerical primary vortex in both radial and axial directions, it will make the formation of smaller vortices unlikely. For computational details such as grid resolution, refer to the work of Khraibut.[29]

There are two possible causes of the difference between experiments and the Navier–Stokes simulation. The first is the no-slip condition used in Navier–Stokes computations. The no-slip assumption is particularly relevant at the separation point downstream of the leading edge along the expansion surface. The predicted separation point by the Navier–Stokes simulation is approximately 0.7 mm[29] downstream of the expansion surface compared to the separation point of 1.4 ± 0.2 mm for the experiment. The separation point is important as it dictates the shear layer reattachment position at the compression surface, along with the formed vortex size and its internal flow structures. In particular, the slip will have a significant influence on the magnitude of vorticity in the separated flow. Therefore, the closer separation location to the leading edge for the Navier–Stokes computation will generate a separated region of different size and internal vortex features. The second cause for the differences between experiment and Navier–Stokes computations is that the experimental flow may not be fully established as the available flow time is limited by the volume of gas initially in the shock tube. As the computational results are a steady-state solution, the transient behavior of the flow at an equivalent test time could not be determined. Moreover, as the primary vortex location is predicted to migrate downstream with additional flow time,[32] the steady-state solution may reflect this downstream location when not accounting for transient flow behavior. Additionally, the Navier–Stokes computations were two-dimensional simulations that did not consider the aspect ratio of the tick model used in these experiments. Although the aspect ratio of 10 was considered sufficient to assume a nominal two-dimensional flowfield at the model span center—the location of the PLIF measurements—there may be some three-dimensional effects in the experiment that are not accounted for in simulation contributing to the flowfield discrepancy.

The establishment time of the separated flowfield generated by the tick configuration is close to that of a compression corner,[40] which could also contribute to computational and experimental discrepancies. Numerical studies by Tumuklu and Levin[41] have demonstrated the unsteadiness of the tick flowfield, which, according to

their work, does not fully establish until approximately 2 ms after flow arrival. The T-ADFA shock tunnel usable test time is limited compared to this numerically predicted establishment time, having a test time of approximately 600 μs. However, using correlations developed by Holden[40] provides a useful order-of-magnitude estimate of the establishment time, which has been used by various experimenters in shock tunnel facilities.[15,42] Holden's experiments show that the establishment time for base flow separated regions is equal to the time for the external inviscid flow to move a distance equal to a characteristic length of 30–50 base diameters. Two correlations exist for base flows that relate flow establishment time to pressure (T_p) and heat flux (T_Q) to the freestream velocity (U_∞) and the model base diameter, given by

$$\frac{T_p U_\infty}{D} = 27.9 \qquad (6)$$

and

$$\frac{T_Q U_\infty}{D} = 70. \qquad (7)$$

As with base flows, the recirculation region of the tick flowfield is downstream of the model's leading edge, which also includes a shock–boundary layer interaction from the separation shock wave as it contacts the recompressing flow. In order to estimate the establishment time, the sound speed within the recirculation region was determined using the expression

$$a_\delta = \sqrt{\gamma R T_{rec}}, \qquad (8)$$

where γ is the ratio of specific heats, R is the universal gas constant, and T_{rec} is the mean temperature in this recirculation region that was taken from Navier–Stokes simulation data.[29] This calculated sound speed was then used in the expression

$$\frac{t_{est} a_\delta}{L_{sep}} = 1 \qquad (9)$$

to determine the flow establishment time, t_{est}, where the characteristic length, L_{sep}, was taken to be the model expansion surface length (20 mm). The minimum establishment time calculated from this relation was found to be approximately 142 μs. Using Holden's third correlation seen in Eq. (7) and assuming that the base diameter is the vertical distance from the model vertex to the leading edge, which is 10 mm, the maximum establishment time was then more conservatively calculated to be approximately 285 μs. This is significantly shorter than 600 μs available before the mixed driver gas contaminates the test gas, indicating that the tick flowfield could be expected to be at least initially established when probed experimentally.

2. Direct simulation Monte Carlo computation

A similar comparison of only the recirculation flow is now made with a two-dimensional solution calculated by Prakash[30] using the direct simulation Monte Carlo (DSMC) SPARTA code developed by Sandia National Laboratories.[43] This comparison is shown in Fig. 10. This time-resolved computation is at a flow time of 1.25 ms after the flow reaches the exit of the nozzle, which is 250 μs earlier than the experimental measurements. The very large computational cost of the experiment limited the flow time for which the results could be obtained. This difference in flow time has no
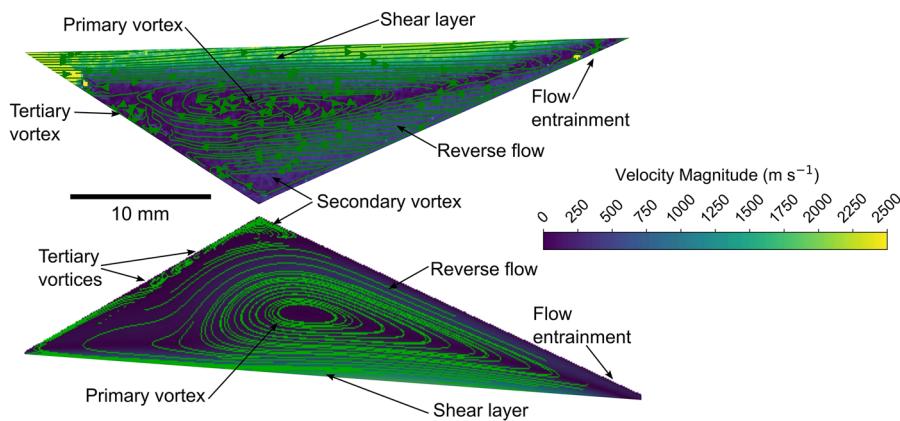
FIG. 10. Experimental separated flow-field streamline map (top) mirrored with equivalent DSMC computation (bottom).

effect on the DSMC comparison with the experiment, as the flow structures do not measurably vary within the 250 μs previous to the plotted time period as shown by Prakash.[30] The modeled leading-edge radius for this calculation is 20 μm, making it nominally match the experiment. As was seen in the Navier–Stokes code comparison, the primary vortex encompasses the majority of the separated region; however, its position here is more horizontally central within the recirculation zone and is offset approximately 4 mm downstream of the corner, which is closer to the location seen in the experiment. In fact, the primary vortex is positioned contrary to what is expected at this flow time of 1.25 ms. The location of this primary vortex should migrate downstream with an increase in flow time,[30] so it would be expected that the center position of the primary vortex would resemble that seen in the experiment. The reverse flow in the DSMC case, as with the Navier–Stokes simulation, follows the compression surface; however, the vertical height of the primary vortex from the shear layer is increased. This, in turn, reduces the apparent size of the DSMC corner secondary vortex or Moffatt eddy that resides in a more central position in reference to the model geometric corner. According to Prakash et al.,[30] this secondary vortex remains approximately aligned with the geometric model corner up to a flow time of 2 ms.

What is captured in the DSMC calculation and is also seen in experiments is the apparent formation of multiple small tertiary vortices on the model expansion surface. These small structures seem to emanate from the secondary vortex and are spatially accommodated by the primary vortex indicated by the bulging streamlines near these smaller vortices. As explained above, this structure is not visible in the steady Navier–Stokes simulations.[29] This could be attributed to the DSMC downstream separation point of approximately 1 mm from the leading edge due to the modeled leading-edge radius difference, as the bluntness of the leading edge has a large influence on the separation point.[30,31] However, further simulation work by Khraibut et al.[29] was carried out using a leading-edge radius of 100 μm, and this also did not show the presence of any tertiary vortices. According to Prakash et al.,[30] these tertiary vortices in the DSMC calculation will amalgamate with further increases in the leading-edge bluntness and wall temperature to form two distinct vortices that are analogous to those seen in the Navier–Stokes results. Overall, there is better agreement between the DSMC calculation of the flowfield and experimental measurements.

Another DSMC calculation of the separated flowfield by Tumuklu and Levin[41] using the SMILE code[44] showed that this amalgamation of the secondary and tertiary vortices will also occur beyond 2 ms of flow time, with the enlarged secondary vortex moving toward the leading edge as seen in the Navier–Stokes computation. Notably, the upstream flow separation point of the DSMC calculation also changes the impingement location of the separation shock wave on the recompression shock downstream. The separation shock impingement location difference between the DSMC computation and the experiment, when taken vertically above the compression surface, is 4 mm. This corresponds to a more obtuse separation shock angle for the experimental measurement by approximately 3°.[41] This coincides with the downstream reattachment point location in the experimental measurement being 6.0 ± 0.2 mm downstream of the DSMC reattachment point.

VI. CONCLUSIONS

This paper has presented a quantitative measurement of a hypersonic leading-edge separation generated by a "tick"-shaped model geometry at a flow condition with a total enthalpy of 3.8 MJ/kg, where the continuum assumption mostly holds. Using the planar laser-induced fluorescence (PLIF) based Doppler-shift velocimetry technique, a two-dimensional velocity map of this flow type has been generated. This map has provided the first direct evidence of the existence of secondary and tertiary vortices in a hypersonic separated flow, as opposed to indirect means such as oil flow visualization or pressure/heat flux measurements. Inspection of the velocity magnitude map produced from two discrete measurements of orthogonal velocity components indicated the separation point to be approximately 1.4 ± 0.2 mm downstream of the leading edge. This separation point did not correspond with the location predicted by both Navier–Stokes and direct simulation Monte Carlo (DSMC) computational codes that were seen to be at 0.7 mm and 1.0 mm closer to the leading edge, respectively. As a consequence of the difference in the separation point, the experimentally measured flow structures deviated from simulations in terms of position particularly within the recirculating flow, along with the wake neck and recompression flow thickness. In the Navier–Stokes comparison, the difference in flow structures is possibly due to the velocity slip at the surface in experimental measurements. Slip effects are not

modeled in the Navier–Stokes solution due to the assumed no-slip condition, which affects the surface shear stress and heat flux downstream leading to a difference in flow structures. The DSMC solution comparison is closer to the experiment, which was due to its superior ability to characterize separation by modeling the strong viscous interactions and localized rarefaction at the leading edge.

The measured velocity magnitudes largely agreed with the computations; however, the freestream was found to be non-uniform, which was due to poor line shape fits to some pixels in a region near the model compression surface. These poor fits were hypothesized to originate from images acquired using a set of UV specific mirrors that are mounted on the shock tunnel for the axial velocity experiment warping during a run of the facility, changing the laser sheet orientation. The peak freestream velocity matched the predicted velocity by using the one-dimensional nozzle code STUBE.

The dividing streamline velocity was quantified in this work, which is an important parameter to investigate using the tick geometry, as it prescribes the quantity of flow that is entrained into the recirculation region and the proportion that flows downstream of the reattachment. Laminar mixing theory presented by Chapman[36] states that, for a leading-edge separation, the dividing streamline velocity, U_{DSL}, between the inviscid freestream and viscous recirculating flow remains constant and has a specific velocity ratio to that of the freestream, U_∞, of $U_{DSL}/U_\infty = 0.587$. In this study, there was a small but finite boundary layer prior to the flow separation. An extension of Chapman's model by Baum and Denison,[38] which includes a finite-thickness boundary layer, was more applicable for comparison with theory. Using this model, a velocity ratio of $U_{DSL}/U_\infty = 0.511$ was found to match that of the mean experimental velocity ratio across the dividing streamline length. It was seen that Chapman's ratio was still within the experimental dividing streamline velocity ratio uncertainty. The closer agreement for this ratio with Chapman's theory than the work done by Hruschka *et al.*[12] for a base flow indicated that the study using the tick model geometry better reflects the assumptions inherent to Chapman's theory.

ACKNOWLEDGMENTS

DATA AVAILABILITY

The data that support the findings of this study are available from the corresponding author upon reasonable request.

REFERENCES

[1]N. Deepak, S. Gai, and A. Neely, "High-enthalpy flow over a rearward-facing step—A computational study," J. Fluid Mech. **695**, 405–438 (2012).

[2]A. Chpoun, "Hypersonic transitional flow in a compression corner in 2D configuration," in *Laminar-Turbulent Transition* (Springer, 1990), pp. 533–543.

[3]C. F. Dewey, "Near wake of a blunt body at hypersonic speeds," AIAA J. **3**, 1001–1010 (1965).

[4]D. Chapman, D. Kuehn, and H. Larson, "Investigation of separated flows in supersonic and subsonic streams with emphasis on the effect of transition," NACA Report 1356, 1958.

[5]T. Kaseman, L. Le Page, S. O'Byrne, H. Kleine, and S. Gai, "Comparison of density-sensitive and fluorescence visualization in low-density separated flow," AIP Conf. Proc. **1786**, 060001 (2016).

[6]T. P. Kaseman, L. M. Le Page, S. B. O'Byrne, and S. L. Gai, "Visualization and thermometry in hypersonic wedge and leading-edge separated flows," in *55th AIAA Aerospace Sciences Meeting* (AIAA, 2017), p. 0443.

[7]B. Melcher, R. Taylor, and W. Washburn, "Studies of the luminous hypersonic wake," AIAA J. **2**, 1731–1738 (1964).

[8]R. Slattery and W. Clay, "Measurement of turbulent transition, motion, statistics, and gross radial growth behind hypervelocity objects," Phys. Fluids **5**, 849–855 (1962).

[9]P. M. Danehy, P. Mere, M. J. Gaston, S. O'Byrne, P. C. Palma, and A. F. P. Houwing, "Fluorescence velocimetry of the hypersonic, separated flow over a cone," AIAA J. **39**, 1320–1328 (2001).

[10]E. Cecil and J. McDaniel, "Planar velocity and temperature measurements in rarefied hypersonic flow using iodine LIF," in *38th AIAA Thermophysics Conference* (AIAA, 2005), p. 4695.

[11]B. Hiller and R. K. Hanson, "Simultaneous planar measurements of velocity and pressure fields in gas flows using laser-induced fluorescence," Appl. Opt. **27**, 33–48 (1988).

[12]R. Hruschka, S. O'Byrne, and H. Kleine, "Two-component Doppler-shift fluorescence velocimetry applied to a generic planetary entry probe model," Exp. Fluids **48**, 1109–1120 (2010).

[13]R. Cattolica and S. Vosen, "Two-dimensional measurements of the [OH] in a constant volume combustion chamber," Symp. (Int.) Combust. **20**, 1273–1282 (1985), Twentieth Symposium (International) on Combustion.

[14]A. C. Eckbreth, *Laser Diagnostics for Combustion Temperature and Species* (CRC Press, 1996), Vol. 3.

[15]M. P. Lee, B. K. McMillin, and R. K. Hanson, "Temperature measurements in gases by use of planar laser-induced fluorescence imaging of NO," Appl. Opt. **32**, 5379–5396 (1993).

[16]J. O. Berg and W. L. Shackleford, "Rotational redistribution effect on saturated laser-induced fluorescence," Appl. Opt. **18**, 2093–2094 (1979).

[17]R. Miles, C. Cohen, J. Connors, P. Howard, S. Huang, E. Markovitz, and G. Russell, "Velocity measurements by vibrational tagging and fluorescent probing of oxygen," Opt. Lett. **12**, 861–863 (1987).

[18]P. M. Danehy, S. O'Byrne, F. P. Houwing, J. S. Fox, and D. R. Smith, "Flow-tagging velocimetry for hypersonic flows using fluorescence of nitric oxide," AIAA J. **41**, 263–271 (2003).

[19]B. Hiller, R. A. Booman, C. Hassa, and R. K. Hanson, "Velocity visualization in gas flows using laser-induced phosphorescence of biacetyl," Rev. Sci. Instrum. **55**, 1964–1967 (1984).

[20]R. Sánchez-González, R. D. W. Bowersox, and S. W. North, "Vibrationally excited no tagging by NO($A^2 \Sigma^+$) fluorescence and quenching for simultaneous velocimetry and thermometry in gaseous flows," Opt. Lett. **39**, 2771–2774 (2014).

[21]R. Miles, "Femtosecond laser electronic excitation tagging (FLEET) for imaging flow structure in unseeded hot or cold air or nitrogen," in *51st AIAA Aerospace Sciences Meeting Including the New Horizons Forum and Aerospace Exposition* (AIAA, 2013), p. 340.

[22]M. Zimmermann and R. B. Miles, "Hypersonic-helium-flow-field measurements with the resonant Doppler velocimeter," Appl. Phys. Lett. **37**, 885–887 (1980).

[23]J. C. McDaniel, B. Hiller, and R. K. Hanson, "Simultaneous multiple-point velocity measurements using laser-induced iodine fluorescence," Opt. Lett. **8**, 51–53 (1983).

[24]B. Hiller, J. C. McDaniel, E. C. Rea, and R. K. Hanson, "Laser-induced fluorescence technique for velocity field measurements in subsonic gas flows," Opt. Lett. **8**, 474–476 (1983).

[25]F. K. Lu and D. E. Marren, *Advanced Hypersonic Test Facilities* (AIAA, 2002), Vol. 198.

[26]C. Mundt, R. Boyce, P. Jacobs, and K. Hannemann, "Validation study of numerical simulations by comparison to measurements in piston-driven shock-tunnels," Aerosp. Sci. Technol. **11**, 100–109 (2007).

[27]R. Stalker, "A study of the free-piston shock tunnel," AIAA J. **5**, 2160–2165 (1967).

[28]I. Vardavas, "Modelling reactive gas flows within shock tunnels," Aust. J. Phys. **37**, 157–178 (1984).

[29]A. Khraibut, S. Gai, L. Brown, and A. Neely, "Laminar hypersonic leading edge separation—A numerical study," J. Fluid Mech. **821**, 624–646 (2017).

[30]R. Prakash, S. Gai, and S. O'Byrne, "A direct simulation Monte Carlo study of hypersonic leading-edge separation with rarefaction effects," Phys. Fluids **30**, 063602 (2018).

[31]A. Khraibut, S. Gai, and A. J. Neely, "Numerical investigation of bluntness effects on hypersonic leading edge separation," in *53rd AIAA Aerospace Sciences Meeting* (AIAA, 2015), p. 0984.

[32]R. Prakash, S. L. Gai, and S. B. O'Byrne, "DSMC computations of separation over a 'tick' model in hypersonic high enthalpy transitional flows," in *55th AIAA Aerospace Sciences Meeting* (AIAA, 2017), p. 1844.

[33]J. M. Seitzman, R. K. Hanson, P. DeBarber, and C. Hess, "Application of quantitative two-line OH planar laser-induced fluorescence for temporally resolved planar thermometry in reacting flows," Appl. Opt. **33**, 4000–4012 (1994).

[34]R. Prakash, L. Le Page, L. McQuellin, S. Gai, and S. O'Byrne, "Direct simulation Monte Carlo computations and experiments on leading-edge separation in rarefied hypersonic flow," J. Fluid Mech. **879**, 633–681 (2019).

[35]P. S. Lykoudis, "A review of hypersonic wake studies," AIAA J. **4**, 577–590 (1966).

[36]D. R. Chapman, "Laminar mixing of a compressible fluid," NACA-TN-1800, 1949.

[37]J. Herrin and J. Dutton, "Supersonic base flow experiments in the near wake of a cylindrical afterbody," AIAA J. **32**, 77–83 (1994).

[38]E. Baum and M. Denison, "Compressible free shear layer with finite initial thickness," AIAA J. **1**, 342–349 (1963).

[39]I. Nompelis and G. V. Candler, "US3D predictions of double-cone and hollow cylinder-flare flows at high-enthalpy," in *44th AIAA Fluid Dynamics Conference* (AIAA, 2014), p. 3366.

[40]M. S. Holden, "Establishment time of laminar separated flows," AIAA J. **9**, 2296–2298 (1971).

[41]O. Tumuklu and D. A. Levin, "On the temporal evolution in laminar separated boundary layer shock-interaction flows using DSMC," AIAA Paper 2017-1614, 2017.

[42]C. Goyne, R. Stalker, and A. Paull, "Skin-friction measurements in high-enthalpy hypersonic boundary layers," J. Fluid Mech. **485**, 1–32 (2003).

[43]M. A. Gallis, J. R. Torczynski, S. J. Plimpton, D. J. Rader, and T. Koehler, "Direct simulation Monte Carlo: The quest for speed," AIP Conf. Proc. **1628**, 27–36 (2014).

[44]M. Ivanov, G. Markelov, and S. Gimelshein, "Statistical simulation of reactive rarefied flows-numerical approach and applications," in *7th AIAA/ASME Joint Thermophysics and Heat Transfer Conference* (AIAA, 1998), p. 2669.